Analysis and modeling of a silicon nitride slot-waveguide microring resonator biochemical sensor

Carlos Angulo Barrios*
Instituto de Sistemas Optoelectrónicos y Microtecnología (ISOM), Universidad Politécnica de Madrid (UPM), Ciudad Universitaria, Madrid, Spain

ABSTRACT

The performance of a recently demonstrated silicon nitride slot-waveguide microring resonator biochemical sensor is analyzed. The slot-waveguide sensor is optically modeled by using finite element method, full-vectorial and semi-vectorial finite-difference beam propagation methods. Numerical calculations are discussed and compared to the sensor experimental performance. This study includes homogeneous sensing -by using different aqueous solutions-, surface sensing -due to both, surface etching and biomolecular layer adhesion-, and power coupling characteristics of the microring sensor. It is found that all of the aforementioned numerical methods provide good agreement with the experimental homogeneous sensitivity, surface etching sensitivity and power transmission coefficient at the resonator coupling. The analysis of the surface sensitivity due to biomolecular layer adhesion suggests biomolecule polymerization on the surface of the actual device. These results demonstrate the suitability of the proposed numerical optical models and indicate that the slot-waveguide microring device can be fully wetted with aqueous analytes, which is desirable for sensing and optofluidic applications at the nanoscale.

Keywords: Integrated optics, silicon photonics, optical sensors, device modeling

INTRODUCTION

Optical refractive index (RI) sensors are extensively investigated for a number of applications and play a prominent role in chemical and biochemical analysis [1,2]. This label-free sensing paradigm can provide real-time results with minimal sample preparation. In RI biochemical sensors, a fraction of an optical probe interacts with the sample to be tested. A change in RI of the probed region causes a corresponding phase shift that can be detected as either a frequency or an intensity shift -by using an interferometric structure- which is converted to the sensing signal. For applications requiring the analysis of a liquid sample (homogeneous sensing), the sensing signal can be employed to determine the RI of the sample as compared to a reference sample. For biomolecule detection applications (surface sensing), the specific capture of biomolecules at the sensor surface results in a local change in RI which produces a sensing signal that enables quantification of the biomolecules in the sample.

Among the existing biological and chemical RI sensors, those based on integrated optical waveguides have been demonstrated to posses promising performances. These devices include planar optical-waveguide sensors [3], directional coupler sensors [4], Mach-Zehnder interformeters [5], grating-coupled waveguides [6], and microresonators [7-12]. Integrated guided-wave devices present important advantages such as high sensitivity, small weight and size, robustness, high surface specificity using surface chemical modifications, easy patterning of reagents and high scale integration with electronic and photonic devices. In addition, they are compatible with microfluidic handling and can accommodate multichannel (multianalyte) sensing.

We have recently demonstrated an integrated biochemical microring RI sensor based on slot-waveguides [11,12]. A slot-waveguide consists of two strips (rails) of a high index material separated by a sub-micrometer low-index (slot) region. By using the electric (E)-field discontinuity at the interface between high-index-contrast materials, high optical intensity can be obtained in the slot region [13]. This remarkable characteristic makes the slot-waveguide very attractive for RI biochemical sensing due to its capability to enhance sample-probe interaction, as reported for the first time in [11] for homogenous sensing, and [12] for surface sensing. For the device demonstrated in those works, Si_3N_4 was employed

*cbarrios@die.upm.es; phone +34 91 549 5700; fax +34 914533567; www.isom.upm.es

Optical Sensors 2009, edited by Francesco Baldini, Jiri Homola, Robert A. Lieberman, Proc. of SPIE Vol. 7356, 735605 · © 2009 SPIE · CCC code: 0277-786X/09/$18 · doi: 10.1117/12.820172

Downloaded from SPIE Digital Library on 06 Jan 2010 to 159.226.100.225. Terms of Use: http://spiedl.org/terms

to implement the high-refractive index rails of the slot-waveguide. The use of Si_3N_4, instead of Si, as the high-index material permits to define a wider slot region -due to a weaker optical confinement in the rails- as compared to the Si case, while maintaining single-mode propagation [14]. A wider slot region facilitates filling the slot volume with liquids for sensing and optofluidic applications [15]. The device sensor was operated at wavelengths around 1.3 μm. This value was chosen because it is commonly employed in telecomm applications (O-band) and the optical absorption of water at 1.3 μm is lower than that at the other common telecom wavelength, 1.55 μm.

In this work, the experimental performance of the biochemical sensor reported in [11] and [12] is analyzed by using photonic device modeling and computer simulations of the optical properties of the Si_3N_4 slot-waveguide ring resonator. The purpose of this study is two-fold: 1) to evaluate the capability of three different numerical methods -commonly used in photonic device design- to model both the homogeneous and surface sensitivities of the sensor under consideration, and 2) to extract relevant information regarding the optofluidic and sensing properties of the device. Next section describes the device model, computation methods and equations used for the analysis. Then, simulation results on the estimation of the sensor bulk and surface sensitivities, and on the coupling characteristics of the microring sensor are presented and discussed. Finally, a summary is given in the last section.

OPTICAL MODEL

Fig. 1a shows a schematic top view of the studied Si_3N_4 slot-waveguide ring resonator. A straight slot-waveguide (bus) is used to couple light into a slot-waveguide ring of radius R=70 μm. Bus and ring are separated by g (coupling distance). Fig. 1b illustrates a schematic cross-section of the bus-ring coupling region. Both bus and ring slot-waveguides consist of two 300-nm-thick (h) Si_3N_4 strips (rails) on a SiO_2 bottom cladding layer. The top of the whole device (cover) is exposed to the environment, that is, the top cladding region (refractive index=n_B) constitutes the sensing region. The inner and outer rails widths of the ring slot-waveguide are w_{r1} and w_{r2}, respectively (asymmetric slot-waveguide), whereas the width of the bus slot-waveguide rails is w_r (symmetric slot-waveguide). The separations between the rails (slot-regions widths) are w_{s1} and w_{s2} for the ring and bus slot-waveguides, respectively. The Si_3N_4 rails are placed on SiO_2 pedestals of height p and widths equal to those of the corresponding Si_3N_4 rails. These pedestals represent an overetching of the SiO_2 bottom cladding layer resulting from the Si_3N_4 rails formation [11].

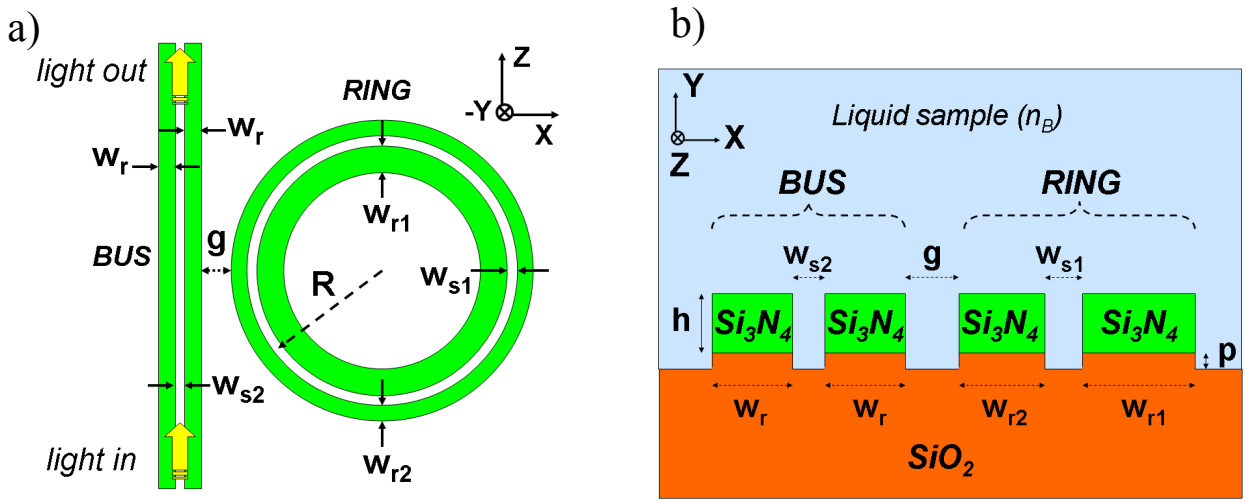

Fig. 1. a) Schematic top view of the Si_3N_4 slot-waveguide ring sensor. b) Schematic cross-section of the coupling region.

To model surface sensing, two cases have been considered: 1) surface sensing due to material removal by highly diluted (1%) HF, and 2) surface sensing due to adhesion of a layer of glutaraldehyde. This is because in the experimental surface sensitivity characterization of the actual device [12], an HF (1%) etching treatment was carried out prior to the adhesion of a glutaraldehyde layer on the sensor surface. Figs. 2a and 2b show schematic cross-sections of the ring slot-waveguide models used to analyze surface etching and biomolecule layer adhesion sensitivities, respectively. In both cases, deionized (DI) H_2O is the ambient material. In Fig. 2a, isotropic HF etching is assumed, with e_{SiO} and e_{SiN} being the

Downloaded from SPIE Digital Library on 06 Jan 2010 to 159.226.100.225. Terms of Use: http://spiedl.org/terms

etching depths in the SiO_2 and Si_3N_4 regions, respectively. Fig. 2b illustrates a glutaraldehide layer, which has been considered to be uniform, of thickness t, adhered to the HF-treated photonic structure. It is also assumed that the adhesion of the biomolecular layer is selective, that is, it only occurs on the Si_3N_4 surface [12]. Values of the main parameters employed in the simulations are collected in Table I. Device dimensions were determined by scanning electron microscope (SEM) measurements on the actual device [11,12].

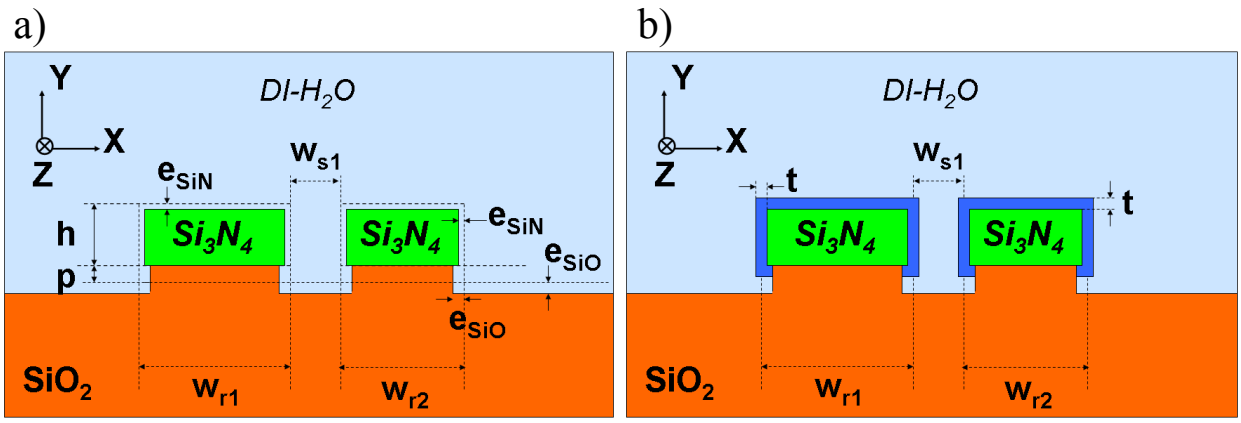

Fig. 2. Schematic cross-sections of the ring slot-waveguide models for surface etching (a) and layer adhesion (b) analysis.

Table 1. Materials parameters and dimensions used in the simulations.

SiO_2 refractive index (λ=1.3μm)	1.445[a]
Si_3N_4 refractive index (λ=1.3 μm)	1.990[a]
DI-H_2O refractive index (λ=1.3 μm)	1.320[b]
Glutaraldehyde refractive index (λ=1.3 μm)	1.466[c]
w_{r1} (nm)	540[d]
w_{r2} (nm)	380[d]
w_r (nm)	400[d]
w_{s1} (nm)	210[d]
w_{s2} (nm)	200 [d]
h (nm)	300[a]
p (nm)	20[d]
g (nm)	250[d]
R (μm)	70
SiO_2 etching rate in HF 1% (nm/min)	6.6[e]
Si_3N_4 etching rate in HF 1% (nm/min)	0.3[f]

(a) From optical measurements
(b) From Ref. 17
(c) From Ref. 18
(d) From SEM measurements
(e) From Ref. 19
(f) From Ref. 20

The device was modeled by using three different three-dimensional (3D) numerical methods: finite element method (FEM), full-vectorial finite-difference beam propagation method (FV-FD-BPM) and semi-vectorial finite-difference beam propagation method (SV-FD-BPM). A commercial photonic design software package from Rsoft [16] was employed for the simulations. For the homogeneous sensitivity analysis, the minimum computation grid sizes along both X-axis and Y-axis were $\Delta x=\Delta y=5$ nm, and the simulation domain was $x\in[-1.5,1.5]$, $y\in[-1.5,1.5]$. For the surface sensitivity analysis, the minimum computation sizes along the X-axis and Y-axis were $\Delta x=2$ nm and $\Delta y=1$ nm, respectively, and the simulation domain was $x\in[-1,1]$, $y\in[-0.6,0.7]$. Perfectly matched layer (PML) for FEM, and

Downloaded from SPIE Digital Library on 06 Jan 2010 to 159.226.100.225. Terms of Use: http://spiedl.org/terms

transparent boundary condition (TBC) for both, FV-FD-BPM and SV-FD-BPM, were used as field conditions at the boundaries of the simulation domains. Bus-ring power coupling was simulated by SV-FD-BPM with a compute step along the propagation direction, Z, of Δz=10 nm.

The microring sensor bulk (homogeneous) sensitivity can be expressed as:

$$S_B = \frac{\Delta\lambda_r}{\Delta n_B} = \frac{\Delta\lambda_r}{\Delta n_{eff}} \frac{\Delta n_{eff}}{\Delta n_B} \tag{1}$$

where λ_r is the microring resonance wavelength and n_{eff} is the effective index of the ring mode. The resonance wavelength incremental change ($\Delta\lambda_r/\Delta n_{eff}$) can be analytically estimated by using the analysis of tuning of microresonators proposed in [21]. For our slot-waveguide microring sensor the cavity mode phase propagation constant (β) in the unperturbed state ($n_B=n_{B0}$, $\lambda_r=\lambda_{r0}$) can be written as:

$$\beta[n_{eff}(n_{B0}, \lambda_{r0})] = \beta_0 \tag{2}$$

where β_0 is the phase constant associated to the resonance wavelength λ_{r0}. As a result of a bulk index perturbation ($n_B=n_{B0}+\Delta n_B$), the phase constant β_0 can be expressed as:

$$\beta[n_{eff}(n_{B0} + \Delta n_{B0}, \lambda_{r0} + \Delta\lambda_r)] = \beta_0 \tag{3}$$

where $\Delta\lambda_r$ is the resonance wavelength shift due to Δn_B. A linear approximation in the effective index, n_{eff}, (sensing parameter), and in the wavelength leads to (Taylor´s formula):

$$\beta[n_{eff}(n_{B0} + \Delta n_{B0}, \lambda_{r0} + \Delta\lambda_r)] \cong \beta[n_{eff}(n_{B0}, \lambda_{r0})] + \Delta n_{eff} \left.\frac{\partial\beta}{\partial n_{eff}}\right|_{\substack{\lambda_r=\lambda_{r0} \\ n_{eff}=n_{eff}(n_{B0},\lambda_{r0})}} + \Delta\lambda_r \left.\frac{\partial\beta}{\partial\lambda}\right|_{\substack{\lambda_r=\lambda_{r0} \\ n_{eff}=n_{eff}(n_{B0},\lambda_{r0})}} \tag{4}$$

where $\Delta n_{eff}=[n_{eff}(n_{B0}+\Delta n_B, \lambda_{r0}+\Delta\lambda_r)- n_{eff}(n_{B0}, \lambda_{r0})]$. From Eq. 4, the shift in the resonant wavelength, $\Delta\lambda_r$, can be written as:

$$\Delta\lambda_r = -\Delta n_{eff} \left.\frac{\partial\beta}{\partial n_{eff}}\right|_{\substack{\lambda_r=\lambda_{r0} \\ n_{eff}=n_{eff}(n_{B0},\lambda_{r0})}} \cdot \left(\left.\frac{\partial\beta}{\partial\lambda}\right|_{\substack{\lambda_r=\lambda_{r0} \\ n_{eff}=n_{eff}(n_{B0},\lambda_{r0})}} \right)^{-1} \tag{5}$$

that is:

$$\Delta\lambda_r = -\Delta n_{eff} \frac{2\pi}{\lambda_{r0}} \cdot \left(-\frac{2\pi n_g(\lambda_{r0})}{\lambda_{r0}^2} \right)^{-1} = \lambda_{r0} \frac{\Delta n_{eff}(\Delta n_B, \Delta\lambda_r)}{n_g(\lambda_{r0})} \tag{6}$$

where $n_g(\lambda_{r0})$ is the group index -which is defined as $n_g= n_{eff} - \lambda(\partial\lambda/\partial n_{eff})$- at the unperturbed resonance wavelength λ_{r0}. The group index can also be estimated from the experimental ring resonator transmission curve as $n_g(\lambda_{r0})\cong\lambda_{r0}^2/[(FSR)L]$, where FSR is the free spectral range (wavelength difference between two consecutive resonance wavelengths) for $n_B=n_{B0}$, and L is the ring length. In our case, the group index of the actual device demonstrated in [11,12] was $n_g(\lambda_{r0}$=1298.45 nm)=1.78 (experimental FSR=2.15 nm).

$\Delta\lambda_r$ in Eq. 6 can be obtained by using the following iterative method. For a given Δn_B, and assuming an initial value of $(\Delta\lambda_r)_0=0$, $\Delta n_{eff}[\Delta n_B,(\Delta\lambda_r)_0]$ is calculated by employing any of the aforementioned numerical methods. The resulting value is inserted in Eq. 6, leading to $(\Delta\lambda_r)_1$. Then Δn_{eff} $[\Delta n_B,(\Delta\lambda_r)_1]$ is again numerically calculated and inserted in Eq. 6, leading to $(\Delta\lambda_r)_2$. This iterative procedure is continued until convergence is achieved, that is, when Δn_{eff} $[\Delta n_B,(\Delta\lambda_r)_n]$ leads to $(\Delta\lambda_r)_{n+1}\cong(\Delta\lambda_r)_n$, which represents the resonant wavelength shift resulting from the bulk fluid refractive index perturbation Δn_B.

Surface sensitivity can be written as:

Downloaded from SPIE Digital Library on 06 Jan 2010 to 159.226.100.225. Terms of Use: http://spiedl.org/terms

$$S_S = \frac{\Delta\lambda_r}{\Delta t} = \frac{\Delta\lambda_r}{\Delta n_{eff}} \frac{\Delta n_{eff}}{\Delta t} \tag{7}$$

where Δt is the thickness variation of an adlayer on the sensor surface. A tuning analysis similar to that described previously leads to:

$$\Delta\lambda_r = \lambda_{r0} \frac{\Delta n_{eff}(\Delta t, \Delta\lambda_r)}{n_g(\lambda_{r0})} \tag{8}$$

for the estimation of the resonance wavelength shift produced by Δt. As done before, $\Delta\lambda_r$ can be calculated for a given Δt by calculating $\Delta n_{eff}(\Delta t, \Delta\lambda_r)$ numerically and solving Eq. 8 iteratively. Note that for the case of surface etching sensitivity (see Fig. 2a), t should be substituted by the etching depths, e_{SiO} and e_{SiN}, which are related to the etching time by the corresponding etching rates given in Table I.

RESULTS AND DISCUSSION

Figs. 3a and 3b show FEM calculations of the major and minor E-fields, respectively, of the fundamental mode of the Si_3N_4 ring slot-waveguide for n_{B0}=1.32 (the ambient material is DI-H_2O) at an operation wavelength of λ_{r0}=1298.45 nm. Simulations revealed single mode operation with the main E-field along the X-axis (quasi-TE polarization). This is in agreement with the experimental characterization of the actual device [11,12], which showed no resonances for quasi-TM polarization (main E-field along the Y-axis).

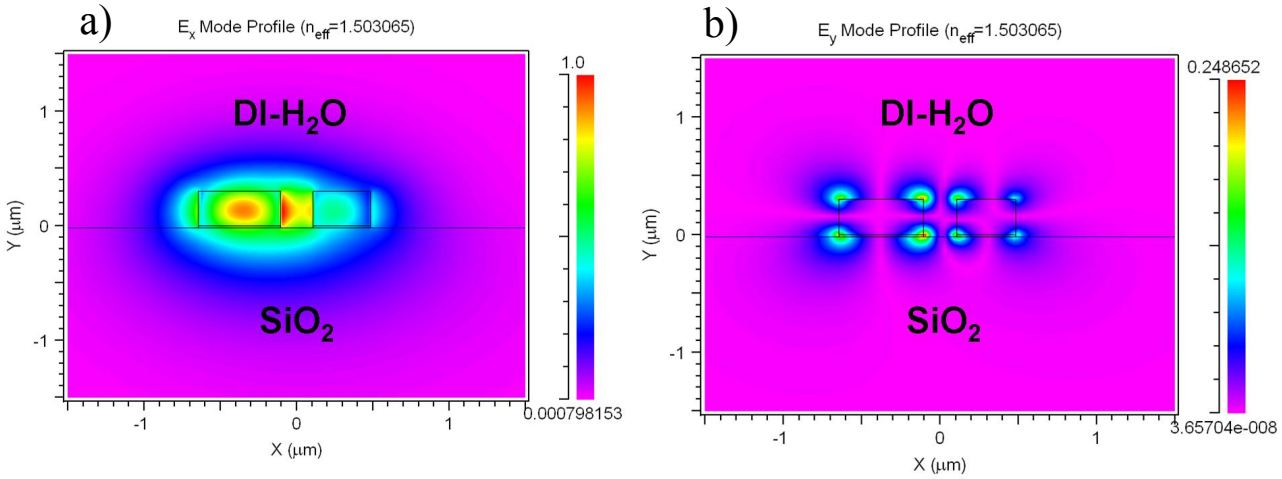

Fig. 3. Finite element method calculations of the major (a) and minor (b) E-field distributions of the fundamental mode of the silicon nitride ring asymmetric-slot-waveguide turning to the left (−X axis) with a radius of curvature of R=70 μm and an operation wavelength of 1298.45 nm.

The fraction of optical power that exists in the bulk sensing region is given by:

$$\eta_B = \frac{\int_B [(E \times H^*) \bullet z] dA}{\int_\infty [(E \times H^*) \bullet z] dA} \tag{9}$$

where **E** is the electric field vector, **H** is the magnetic field vector, **z** is the propagation direction, B alludes to the bulk ambient (sensing) region and the integrals are evaluated over the cross-sectional area of the waveguide. Numerical solving of Eq. 9 led to η_B=0.27 for DI-H_2O as the bulk ambient material.

Downloaded from SPIE Digital Library on 06 Jan 2010 to 159.226.100.225. Terms of Use: http://spiedl.org/terms

1.1 Homogeneous sensing

As reported in [11], the measured ambient bulk wavelength sensitivity of the actual sensor was S_B = 212 nm/RIU (refractive index unit), which was obtained by using different ethanol concentrations in DI-H_2O. Fig. 4 shows the calculated (Eq. 6) and experimental [11] resonance wavelength shifts of the slot-waveguide microring resonator sensor as a function of the bulk fluid refractive index. It is seen that FEM- and FV-FD-BPM-based calculations are nearly identical, whereas SV-FD-BPM provides slightly smaller values than the other two methods. This divergence is expected since both FEM and FV-FD-BPM take into account both polarization components and the coupling between them, while SV-FD-BPM assumes that the transverse field components are decoupled, simplifying the calculation considerably but diminishing the accuracy. In general, the effect of the off-diagonal terms in the vector wave equation defining wave propagation in a slot-waveguide cannot be considered negligible due to the complex geometry of the waveguide, and, therefore, full-vectorial methods are recommended to model slot-waveguides in order to obtain accurate solutions. Nevertheless, Fig. 4 indicates that polarization coupling is not significant in our ring slot-waveguide, and any of the considered numerical methods could be used to design and to analyze homogeneous sensitivity of similar devices as that under study. This could be attributed to the moderate index-contrast existing between Si_3N_4 and SiO_2. For a a lot-waveguide based on a higher index-contrast material system such as Si/SiO_2, the effect of coupling between polarization components can be relevant.

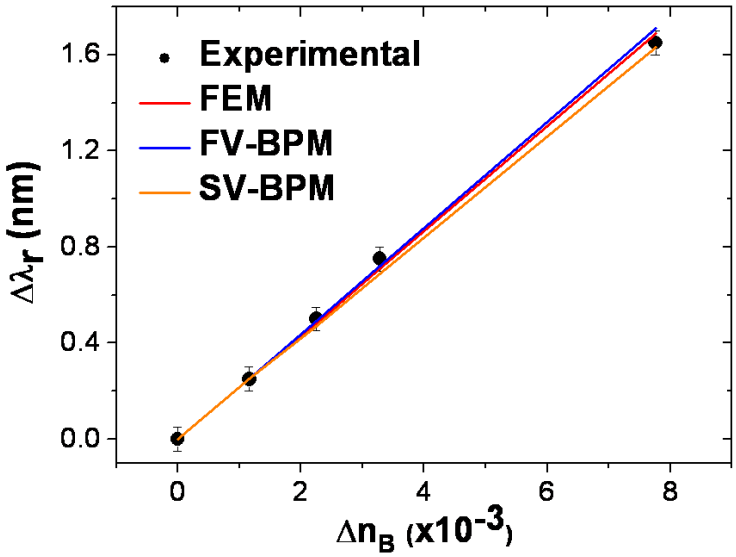

Fig. 4. Calculated and experimental (black dots) resonance wavelength shifts of the silicon nitride slot-waveguide microring sensor as a function of the bulk fluid refractive index variation. Red, blue and orange straight lines correspond to FEM-, FV-FD-BPM- and SV-FD-BPM-based calculations, respectively.

The agreement between the calculations and the experimental results also suggests that the 210-nm-wide slot ring channel is fully filled with the different aqueous solutions employed in the measurements. This is a remarkable conclusion because it demonstrates that the slot-waveguide ring device can be used for optofluidic applications where enhanced light-liquid interaction at the nanoscale is desired.

1.2 Surface sensing

A) Surface etching

Fig. 5 shows the calculated resonance wavelength shifts as a function of the HF etching time. As a consequence of the partial removal of the Si_3N_4 and SiO_2 regions, the effective index of the ring slot-waveguide optical mode decreases and, therefore, the resonance wavelengths are blue-shifted ($\Delta\lambda_r$ is negative). It is observed that both FEM and FV-FD-BPM curves coincide, whereas SV-FD-BPM calculations slightly diverge from the latter as the etching time increases. The experimental resonance variation that resulted after 3 minutes of HF (1%) etching treatment on the actual device was $\Delta\lambda_{r,HF}$ = -1.85 nm**,** which is in excellent agreement with the theoretical curves, as shown in Fig. 5.

Downloaded from SPIE Digital Library on 06 Jan 2010 to 159.226.100.225. Terms of Use: http://spiedl.org/terms

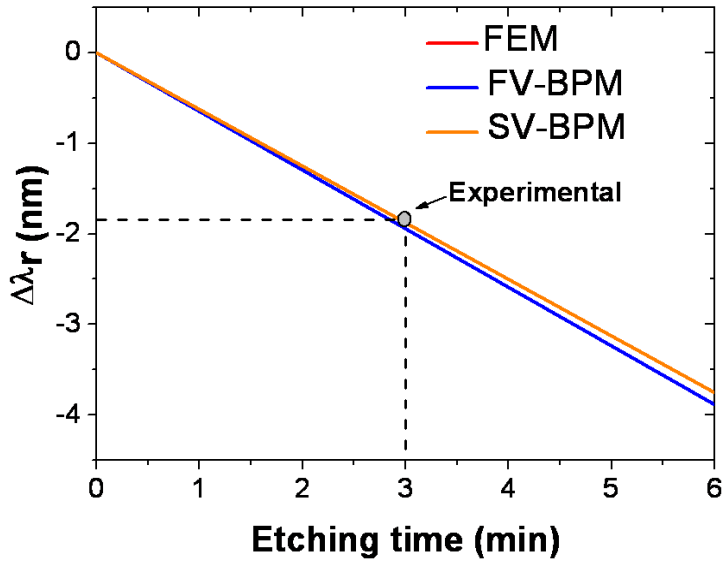

Fig. 5. Calculated resonance wavelength shifts of the silicon nitride slot-waveguide microring sensor as a function of the HF etching time. Red, blue and orange straight lines correspond to FEM-, FV-FD-BPM- and SV-FD-BPM-based calculations, respectively. FEM and FV-BPM curves are overlapped. Experimental data is indicated as a grey dot.

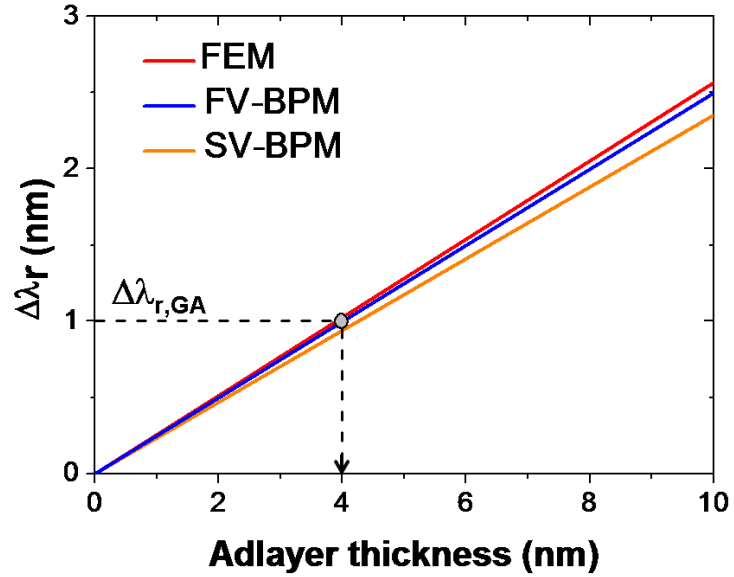

Fig. 6. Calculated resonance wavelength shifts of the slot-waveguide microring sensor as a function of a glutaraldehyde (GA) adlayer thickness. Red, blue and orange straight lines correspond to FEM-, FV-FD-BPM- and SV-FD-BPM-based calculations, respectively. $\Delta\lambda_{r,GA}$ is the experimental resonance shift after 2 hours of GA incubation.

B) Biomolecular adlayer

The calculated resonance wavelength shifts as a function of the thickness of a glutaraldehyde adlayer are shown in Fig. 6. Similar behavior is observed as those found for homogeneous and surface etching sensitivities. That is, FEM and FV-FD-BPM results are nearly equal, while SV-FD-BPM values slightly deviate from the latter as the perturbation (in this

Downloaded from SPIE Digital Library on 06 Jan 2010 to 159.226.100.225. Terms of Use: http://spiedl.org/terms

case, layer thickness) increases. Thus, from a practical perspective, it can be concluded that all of the numerical methods employed in this work provide similar estimations of the effective biomolecule layer thickness for thin adlayers. The experimental wavelength shift that resulted after 2 hours of glutaraldehyde incubation on the actual sensor surface [12] was $\Delta\lambda_{r,GA}$= 1.0 nm. According to the theoretical curves in Fig. 6, such a resonance wavelength shift would correspond to a biomolecular layer thickness of approximately 4 nm. The typical thickness of a monolayer of glutaraldehyde is approximately 2 nm [18]. This difference in thickness could be attributed to polymerization of glutaraldehyde [22] due to the long incubation time [18], which would produce a thicker adhered layer. It should be noted that, in general, an accurate determination of a biomolecule layer thickness is a challenging task due to lack of layer uniformity produced by complex biomolecules morphologies and binding configurations.

1.3 Bus-ring power coupling

From the previous discussion, it has been shown that 3D SV-FD-BPM properly models the sensing behavior of the Si_3N_4 slot-waveguide microring resonator under study. In this section, this method is also used to analyze the power coupling from the bus to the ring (see Fig. 1), with DI-H_2O as the liquid sample. For this purpose, the fundamental mode of the bus slot-waveguide was launched in the bus waveguide, and the field distribution of the propagating beam was calculated, as shown in Fig. 7a. A numerical monitor was used to record the evolution of the power in the bus slot-waveguide (including both rails and slot region) along the propagation direction, Z (Fig. 7b). It is seen in Fig. 7 that a fraction of the launched input power (P_{in}) is coupled into the ring and, therefore, the output power in the bus, P_{out}, decreases. The power transmission coefficient $|r|^2$ at the waveguide resonator coupling can be calculated as $|r|^2 = P_{out}/P_{in}$, which resulted to be $|r|^2 = 0.626$.

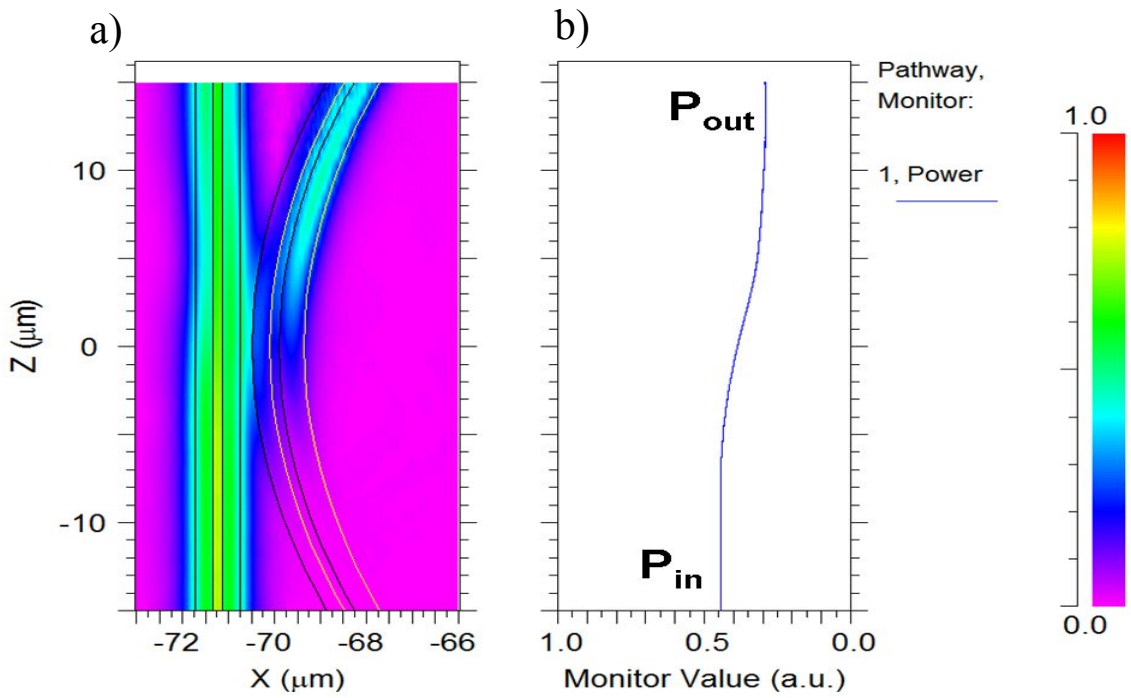

Fig. 7. SV-FD-BPM calculation of light propagation in the coupling region of the slot-waveguide ring sensor for n_B=1.32 (DI-H_2O). a) E_x-field distribution. The fundamental mode of the bus slot-waveguide is launched at Z=-15 μm. b) Evolution of the power in the bus slot-waveguide along the propagation direction (Z-axis).

From the experimental spectral transmittance of the ring reported in [11] for DI-H_2O cover, the power transmission coefficient $|r|^2$ can be extracted by fitting the measured resonance curve with the well-known amplitude function transfer of a ring resonator [14]:

Downloaded from SPIE Digital Library on 06 Jan 2010 to 159.226.100.225. Terms of Use: http://spiedl.org/terms

$$T_{ring}(\lambda) = \frac{a^2 + r^2 - 2ar\cos\left(\frac{2\pi L n_{eff}}{\lambda}\right)}{1 + a^2 r^2 - 2ar\cos\left(\frac{2\pi L n_{eff}}{\lambda}\right)} \tag{10}$$

with $a = \exp-(\alpha L/2)$, where a is the inner circulation factor, α is the total loss in the ring and L is the ring length. From this fit (Fig. 8), a=0.513 and $|r|^2$=0.617, which agrees well with the value calculated by SV-FD-BPM ($|r|^2$=0.626). This evidences full filling of the coupling region and the bus slot-nanochannel with DI-H_2O.

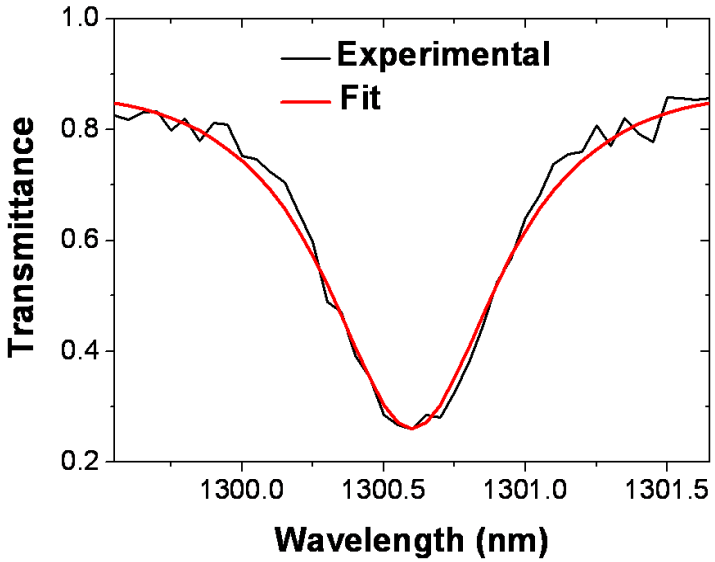

Fig. 8. Experimental transmittance (black line) and theoretical fit (red line) of the slot-waveguide microring resonator at resonance.

SUMMARY

In this work, a recently demonstrated Si_3N_4/SiO_2 slot-waveguide microring RI integrated sensor has been modeled and analyzed. FEM, FV-FD-BPM and SV-FD-BPM numerical methods have been used to calculate the optical characteristics of the photonic structure and to estimate the homogeneous and surface (due to both, surface etching and biomolecule layer adhesion) sensitivities of the sensor. It has been found that FEM and FV-FD-BPM provide nearly identical results whereas SV-FD-BPM values slightly diverge from the latter as the analyte perturbation increases. From a practical point of view, this divergence is not significant, and all of the considered numerical procedures give good estimations of the device sensitivities when compared to the experimental performance of the actual sensor. There are good agreements between calculations and measurements regarding homogeneous sensing (even for ambient refractive index perturbations as large as $8x10^{-3}$ RIU) and surface etching (with HF 1%) sensing. In the case of device surface sensing based on biomolecule (glutaraldehide) layer adhesion, comparison between the experimental and theoretical resonance shifts suggests that the effective thickness of the biomolecular adlayer on the actual device was larger than that of a glutaraldehyde monolayer. This could be attributed to biomolecule polymerization on the sensor surface resulting from a long incubation time. Bus-ring power coupling, with DI-H_2O as the ambient fluid, has also been analyzed by SV-FD-BPM. Calculations agree well with the measured transmission coefficient at the ring resonator coupling, demonstrating the suitability of SV-FD-BPM to model the performance of the sensor under study. The presented results indicate that both, the submicron slot-nanochannels and the coupling region of the device, are fully filled with the aqueous solutions used in the experiments, which makes biochemical sensors consisting of integrated silicon nitride slot-waveguide configurations appropriate for a wide range of optofluidic applications based on simultaneous confinement of light and liquids at the nanoscale.

Downloaded from SPIE Digital Library on 06 Jan 2010 to 159.226.100.225. Terms of Use: http://spiedl.org/terms

ACKNOWLEDGEMENT

The author acknowledges Dr. M.J. Bañuls and V. González-Pedro for useful discussions. This work was funded by the Spanish Ministry of Science and Innovation under project TEC2008-06574-C03-03.

REFERENCES

[1] S. Balslev, A.M. Jorgensen, B. Bilenberg, K.B. Mogensen, D. Snakenborg, O. Geschke, J.P. Kutter, and A. Kristensen, "Lab-on-a-chip with integrated optical transducers," Lab on a Chip 6, 213 (2006).

[2] I.M. White and X. Fan, "On the performance quantification of resonant refractive index sensors," Opt. Express, 16 (2), 1021 (2008).

[3] T. Okamoto, M. Yamamoto, and I. Yamaguchi, "Optical waveguide absorption sensor using a single coupling prism," J. Opt. Soc. Amer. A **17**, 1880-1886 (2000).

[4] B.J. Luff, R.D. Harris, and J.S. Wilkinson, "Integrated-optical directional coupler biosensor," Opt. Lett. **21**, 618-620 (1996).

[5] R.G. Heideman, R.P.H. Kooyman, and J. Greve, "Performance of a highly sensitive optical waveguide Mach-Zehnder interferometer immunosensor," Sensors Actuators B **10**, 209-217 (1993).

[6] R. Hornath, H.C. Pedersen, N. Skivesen, D. Selmeczi, and N.B. Larsen, "Optical waveguide sensor for on-line monitoring of bacteria," Opt. Lett., 28 (14), 1233-1235 (2003).

[7] H. Sohlström and M. Öberg, "Refractive Index Measurement Using Integrated Ring Resonators," 8th European Conference on Integrated Optics (EICO'97), 322-325 (1997).

[8] E. Krioukov, D.J. Klunder, A. Driessen, J. Greve, and C. Otto, "Sensor based on an integrated optical microcavity," Opt. Lett. 27 (17), 512-514 (2002).

[9] A. Yalçin, K.C. Popat, J.C. Aldridge, T.A Desai, J. Hryniewicz, N. Chbouki, B.E. Little, O. King, V. Van, S. Chu, D. Gill, M. Anthes-Washburn, M.S. Ünlü, B.B. Goldberg, "Optical Sensing of Biomolecules Using Microring Resonators," IEEE J. Sel. Top. Quantum Electron. **12**, 148-155 (2006).

[10] A. Schweinsberg, S. Hocdé, N.N. Lepeshkin, R.W. Boyd, C. Chase and J.E. Fajardo, "An environmental sensor based on an integrated optical whispering gallery mode disk resonator," Sensors Actuators B **123**, 727-732 (2007).

[11] C.A. Barrios, K.B. Gylfason, B. Sanchez, A. Griol, H. Sohlström, M. Holgado and R. Casquel, "Slot-waveguide biochemical sensor," Opt. Lett. **32**, 3080-3082 (2007).

[12] C.A. Barrios, M.J. Bañuls, V. Gonzalez-Pedro, K.B. Gylfason, B. Sánchez, A. Griol, A. Maquieira, H. Sohlström, M. Holgado, and R. Casquel, "Label-free optical biosensing with slot-waveguides," Opt. Lett. **33**, 708-710 (2008).

[13] V. Almeida, Q. Xu, C.A. Barrios, and M. Lipson, "Guiding and confining light in void nanostructure," Opt. Lett. **29**, 1209-1211 (2004).

[14] C. A. Barrios, B. Sánchez, K. B. Gylfason, A. Griol, H. Sohlström, M. Holgado, R. Casquel, "Demonstration of slot-waveguide structures on silicon nitride / silicon oxide platform," Opt. Express **15**, 6846-6856 (2007).

[15] C.A. Barrios, M. Holgado, O. Guarneros, K. B. Gylfason, B. Sánchez,R. Casquel, and H. Sohlström, "Reconfiguration of microring resonators by liquid adhesion," Appl. Phys. Lett. 93, 203114 (2008).

[16] http://www.rsoftdesign.com/

[17] C.-B Kim and C.B. Su, "Measurement of the refractive index of liquids at 1.3 and 1.5 micron using a fibre optic Fresnel ratio meter," Meas. Sci. Technol. 15, 1683-1686 (2004).

[18] M.J. Bañuls (private communication).

[19] H. Kikyuama, N. Miki, K. Saka, J. Takano, I. Kawanabe, M. Miyashita, and T. Ohmi, "Principles of wet chemical processing in ULSI micro fabrication," IEEE Transactions on Semiconductor Manufacturing, **4**, 26-35 (1991).

[20] B. du Bois, G. Vereecke, A. Witvrouw, P. de Moor, C. Van Hoof, A. de Caussemaeker, and A. Vervist, "HF etching of Si-oxides and Si-nitrides for surface micromachining," Proceedings of the Sensor Technology Conference, 131-136, Leuven, Belgium (2001).

[21] M. Hammer, K.R. Hiremath, and R. Stoffer, "Analytical approaches to the description of optical microresonator devices," in Proc. AIP Conf.- Microresonators Building Blocks for VLSI Photonics, M. Bertolotti, A. Driessen, and F. Michelotti, Ed. Melville, NY: Amer. Inst. Phys. **709**, 48-71 (2004).

[22] P. Monsan, G. Puzo, and H. Mazarquil, "Mechanism of glutaraldehyde-protein bond formation," Biochimie **57**, 1281-92 (1975).

Downloaded from SPIE Digital Library on 06 Jan 2010 to 159.226.100.225. Terms of Use: http://spiedl.org/terms